# Nucleate Pool Boiling CFD simulation

Yanis Mondet

December 5, 2024

**Abstract**

This report present the development a CFD simulation for modelling nucleate pool boiling on OpenFOAM. It take place in the course Numerical project at Grenoble INP - ENSE3.

## 1 Introduction

Boiling phenomena occur in a wide range of engineering applications, such as vapor generators in a nuclear power plants. Understanding boiling is crucial for optimizing these systems. However, boiling heat transfert is highly complex and no full comprehensive theory currently describes boiling across all conditions and applications. Boiling heat transfert can be studied at different lenght scales, from individual bubble dynamics to interaction between water and vapor phases.

One approach for simulating boiling is Computational FLuid Dynamics (CFD) simulation. In this project, boiling is studied through numercial simulatiosn at the scale of a single bubble. The open-source software OpenFOAM version V2106 was used, employing and modifying a solver developped [1] and detailled [2] by Municchi and Magnini.

This report first presents an overview of boiling modelling and a description of the numerical model used for this simulation. Then, the bubble detachment studied by Georgoulas et al. [3] is reproduced and the influence of various parameters is studied and their effects is compared on the boiling process.

## 2 Boiling modelling

### 2.1 Basic knowledge about multiphase flow modelling

Since in our case we don't need to folow the bubble we are going to use an Eulerain model. There are two possible model: VOF method or the Euler-Euler model. Firstly, we are going to use the VOF method in order to simulate the flow.

The **Volume of Fluid (VOF)** model is used to track and locate the interface between two immiscible fluids, such as liquid and vapor, in multiphase flow simulations. The VOF model introduces a **volume fraction field** $\alpha$ to represent the presence of each fluid in a computational cell.

The volume fraction $\alpha$ represents the fraction of the cell occupied by the liquid phase:

$$\alpha = \begin{cases} 1, & \text{cell fully liquid} \\ 0, & \text{cell fully vapor} \\ 0 < \alpha < 1, & \text{interface region (mixed cell)} \end{cases}$$

The interface is represented by cells where $0 < \alpha < 1$. In these mixed cells, the interface can be approximated using techniques like the Piecewise Linear Interface Calculation (PLIC), which provides an accurate representation of the boundary between the phases.

In cells containing the interface, the fluid properties such as density $\rho$ and viscosity $\mu$ are computed as weighted averages based on $\alpha$:

$$\rho = \alpha\rho_l + (1-\alpha)\rho_v, \tag{1}$$

$$\mu = \alpha\mu_l + (1-\alpha)\mu_v, \tag{2}$$

where $\rho_l$ and $\mu_l$ are the properties of the liquid phase, and $\rho_v$ and $\mu_v$ are the properties of the vapor phase.

## 2.2 Governing Equation for VOF

### 2.2.1 Volume fraction equation

The volume fraction equation is:

$$\frac{\partial \alpha}{\partial t} + \nabla \cdot (\alpha \mathbf{u}) = -\frac{1}{\rho_1} m_i'' \nabla \alpha$$

where:
- $\alpha$: volume fraction of liquid phase (ranges from 0 for vapor to 1 for liquid),
- $\mathbf{u}$: velocity vector of the flow,
- $m_i''$: phase change rate per unit area (interface mass flux, measured in kg/m$^2$/s),
- $\rho_1$: density of the liquid phase.

This equation describes how the volume fraction of the liquid phase changes due to advection and phase change at the interface.

### 2.2.2 Incompressibility Condition

The incompressibility condition is modified to account for phase change, incorporating densities of both phases:

$$\nabla \cdot \mathbf{u} = \frac{1}{\rho_2} - \frac{1}{\rho_1} m_i'' \nabla \alpha$$

where $\rho_2$ is the density of the vapor phase.
This ensures that the divergence of velocity considers the density difference due to phase transition between liquid and vapor.

### 2.2.3 Energy Equation

The energy conservation equation integrates conductive and convective heat transfer with latent heat effects at the phase boundary:

$$\frac{\partial (\rho c_p T)}{\partial t} + \nabla \cdot (\rho c_p \mathbf{u} T) = \nabla \cdot (\lambda \nabla T) - m_i'' h_{lv} \nabla \alpha$$

where:
- $T$: temperature,
- $c_p$: specific heat capacity,
- $\lambda$: thermal conductivity,
- $h_{lv}$: latent heat of vaporization.

This equation models the thermal behavior of the system, incorporating both the heat diffusion in the bulk phases and the heat required for phase change at the interface.

### 2.2.4 Momentum Conservation (Navier-Stokes Equation)

The momentum equation includes terms for pressure, viscosity, and surface tension at the interface:

$$\frac{\partial (\rho \mathbf{u})}{\partial t} + \nabla \cdot (\rho \mathbf{u} \mathbf{u}) = -\nabla p + \nabla \cdot \tau + \mathbf{F}_\sigma$$

where:
- $p$: pressure,
- $\tau$: viscous stress tensor,
- $\mathbf{F}_\sigma$: surface tension force.

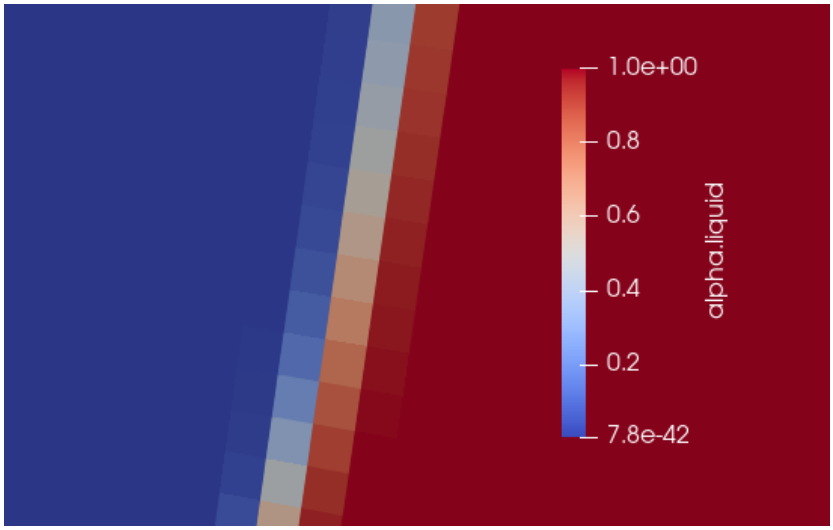


Figure 1: Interface of the bubble

### 2.2.5 VOF methods

Two main Volume of Fluid (VOF) methods have been developed the algebraic and geometric approaches. The main diffences are explained using the review of Mulbah et al.[4]. In algebraic VOF (AVOF) methods, the volume fraction $\alpha$ is represented as a mathematical function, while in geometric VOF (GVOF) methods, $\alpha$ is represented explicitly through interface geometry.

Algebraic methods are relatively easier to implement and more computationally efficient. However, they often create numerical diffusion, require artificial compression schemes, and lose accuracy at high Courant numbers. These methods are generally less accurate compared to geometric methods but are preferred for cases where computational efficiency is a priority.

Geometric methods, on the other hand, offer accurate interface advection and are better suited for preserving sharp interfaces. They work well on unstructured meshes and are preferred for complex flow problems. However, their implementation is computationally intensive, especially in three-dimensional cases, as they require complex geometric operations and reconstructions.

Overall, AVOF methods are efficient for simpler applications, while GVOF methods are more accurate and reliable for challenging simulations involving detailed interface dynamics.

### 2.2.6 Interface Conditions

The **interface indicator function** $I$ specifies the phase (liquid or vapor) at each point, defined as:

$$I(\mathbf{x}, t) = \begin{cases} 1, & \text{in liquid} \\ 0, & \text{in vapor} \end{cases}$$

The volume fraction $\alpha$ is then calculated by integrating $I$ over a control volume $V$:

$$\alpha = \frac{1}{V} \int_V I(\mathbf{x}, t) dV$$

This function determines the local phase within the control volume and guides phase change calculations by indicating where $\alpha$ transitions.

We can see in Figure 1 that for a mesh with 1 micrometer cells, the interface is contained in only three cells. When, talking of a parameter at the interface for instance temperature, we talk about the temperature of the middle cell of the interface.

### 2.2.7 Surface tension force

For the surface tension forec we use the Continuum Surface Force (CSF) model [5] given by:

$$\mathbf{F}_\sigma = 2\frac{\rho}{\rho_l + \rho_v}\sigma\kappa\nabla\alpha$$

where: - $\sigma$: surface tension coefficient, - $\kappa$: interface curvature, - $\rho$: effective density based on the volume fraction, $\rho = \rho_2 + (\rho_1 - \rho_2)\alpha$.

The curvature $\kappa$ of thes surface is calculated using the formula:

$$\kappa = -\nabla \cdot \hat{n}, \tag{3}$$

where $\hat{n}$ is the unit normal vector to the surface. The derivation of this formula can be found in the appendix for completeness.

$$n(x) = \nabla\alpha(x). \tag{4}$$

The unit normal vector is then obtained as:

$$\hat{n}(x) = \frac{\nabla\alpha(x)}{|\nabla\alpha(x)|}. \tag{5}$$

### 2.2.8 Phase Change with the Hardt and Wondra Model

The interfacial mass flux $m_i''$ is modeled according to Hardt and Wondra [6]:

$$m_i'' = \frac{h_i}{h_{lv}}(T_i - T_{sat}) \tag{6}$$

where:

- $T_i$ is the temperature at the interface.
- $T_{sat}$ is the saturation temperature at the interfacial pressure.
- $h_i$ is the interfacial heat transfer coefficient given by:

$$h_i = \left(\frac{2\gamma}{2-\gamma}\right)\rho_v h_{lv}\left(\frac{\bar{M}}{2\pi\bar{R}}\right)^{1/2}\left(\frac{p_v}{T_{sat}^3}\right)^{1/2} \tag{7}$$

- $\gamma$ is an accommodation coefficient (typically between 0 and 1).
- $\bar{M}$ is the molar mass.
- $\bar{R}$ is the universal gas constant.
- $p_v$ is the vapor pressure at the interface.

Together, these equations govern the conservation of phase fraction, momentum, and energy in the "boilingFoam" solver, allowing it to accurately simulate phase change dynamics such as boiling and condensation by resolving heat transfer, interface movement, and density differences across phases.

# 3 Numerical model validation

To validate the solver, a test case included in the solver was tested and subsequently adapted to different configurations, with the results compared to analytical solutions.

## 3.1 Bubble Growth Theory

Bubble growth is a basic test case used to validate multiphase solver, Scriven [7] developed a numerical solution for bubble growth in a saturated liquid. The bubble radius $R(t)$ follows the law:

$$R(t) = 2\beta\sqrt{D\,t}, \tag{8}$$

where $\beta$ is given by:

$$\beta = J_a\sqrt{\frac{3}{\pi}}, \tag{9}$$

and the Jacob number $J_a$ is defined as:

$$J_a = \frac{(T_\infty - T_{\text{sat})}\rho_l c_{p,l}}{\rho_v h_{l,v}}. \tag{10}$$

This boundary layer, derived from thermal diffusion theory (without additional heat sources), is defined by the following equation:

$$\delta = 2\sqrt{Dt}, \tag{11}$$

where $D$ is the thermal diffusivity and $t$ is the time required for the bubble to reach its current size. Using this formula in combination with the Scriven radius equation, we obtain:

$$\delta = \frac{R(t)}{\beta}, \tag{12}$$

where $R$ is the bubble radius and $\beta$ is a growth factor.

## 3.2 Test Cases

### 3.2.1 Definition of General Parameters

After testing the solver with the included test cases, we modified one of them to simulate bubble growth in saturated water with a temperature difference ($\Delta T$) of 5°C. A 2D axisymmetric geometric approach is employed due to limited computational power. A bubble with an initial diameter of 100 $\mu$m is expected to grow to 500 $\mu$m within 2 ms. The initial conditions consist of a vapor bubble at 373.15 K surrounded by liquid at 378.15 K. To ensure both convergence and physical accuracy, the initial thermal boundary layer $\delta$ is added as an initial condition.

The boundary conditions (BC) for this simulation are as follows:

- **Axis (Left Boundary):** Symmetry boundary condition, implying no flux across this boundary. This reduces the computation to half of the domain.
- **Top Boundary:**
  - Fixed value for pressure ($P$)
  - Zero gradient for $\alpha$ (volume fraction), $T$ (temperature), and $U$ (velocity)
- **Right Boundary:**
  - Fixed value for pressure ($P$)
  - Zero gradient for $\alpha$, $T$, and $U$
- **Bottom Boundary:** Symmetry boundary condition

To validate the solver while keeping computation times manageable, we limit the simulation to the first 0.4 ms of growth. This allows for a smaller domain and reduces the overall calculation time. We conduct a mesh convergence analysis using a structured square mesh, as shown in the Figure 2. The domain size is set to $L = 0.5$ mm, ensuring that the bubble remains smaller than half the domain size throughout the simulation.

| **Property** | **Unit** | **Liquid** | **Vapour** |
|---|---|---|---|
| Density, $\rho$ | $\mathrm{kg\,m^{-3}}$ | 958 | 0.597 |
| Specific heat capacity, $c_p$ | $\mathrm{J\,kg^{-1}\,K^{-1}}$ | 4220 | 2030 |
| Thermal conductivity, $k$ | $\mathrm{W\,m^{-1}\,K^{-1}}$ | 0.679 | 0.025 |
| Dynamic viscosity, $\mu$ | $\mathrm{Pa\,s}$ | $2.77 \times 10^{-4}$ | $1.30 \times 10^{-5}$ |
| Heat of vaporization, $h_{lv}$ | $\mathrm{J\,kg^{-1}}$ | 2,257,000 | |
| Surface tension, $\sigma$ | $\mathrm{N\,m^{-1}}$ | 0.059 | |
| Saturation temperature, $T_{\mathrm{sat}}$ | K | 373.15 | |
| Pressure, $P$ | bar | 1.013 | |
| Growth constant, $\beta$ | - | 14.59 | |
| Initial thermal layer thickness, $\delta_{\mathrm{therm}}$ | m | $7.00 \times 10^{-6}$ | |
| Thermal diffusivity, $D$ | $\mathrm{m^2\,s^{-1}}$ | $1.68 \times 10^{-7}$ | |
| Superheat, $\Delta T$ | K | 5 | |
| **Additional Simulation Parameters** | | | |
| Initial bubble diameter | µm | 100 | |
| Target bubble diameter | µm | 500 | |
| Simulation time | ms | 0.4 | |
| Domain size, $L$ | mm | 0.5 | |
| Temperature inside bubble | K | 373.15 | |
| Temperature in liquid | K | 378.15 | |
| Courant number (CFL) | - | 0.2 | |
| Mesh size, $\Delta_x$ | µm | 1–2 | |

Table 1: Summary of Parameters for Bubble Growth Simulation

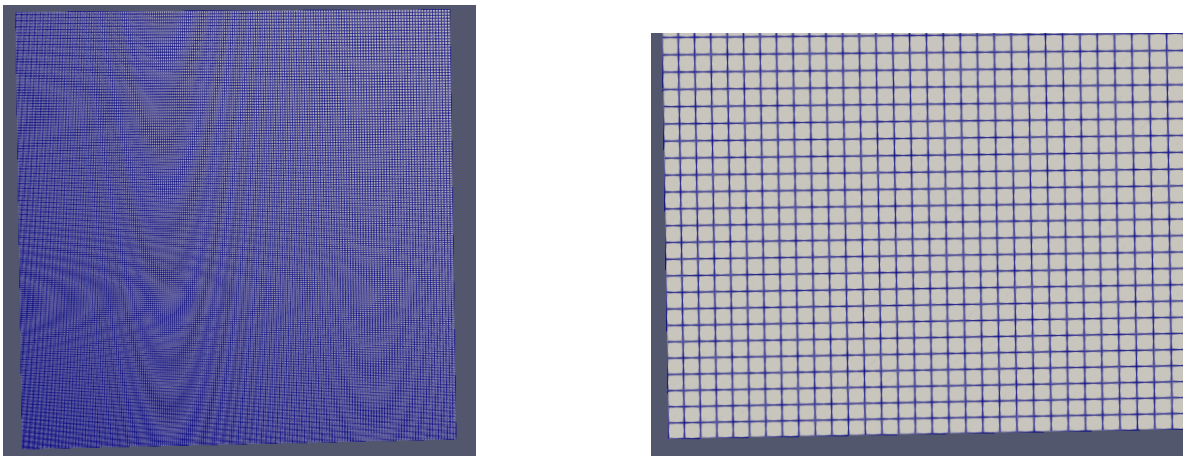

(a) Global Mesh

(b) Local Mesh

Figure 2: Comparison of Global and Local Meshes

A crucial parameter in CFD simulations is the Courant–Friedrichs–Lewy (CFL) number. After testing various Courant numbers, we observed that a CFL of 0.02 provides high accuracy but results in very long computation times. Conversely, a CFL of 1 speeds up the calculation but leads to poor resolution, with deformations observed at the bubble boundary, as shown in the Figure 3.

Ultimately, a Courant number of 0.2 was chosen as a good balance between accuracy and computation time.

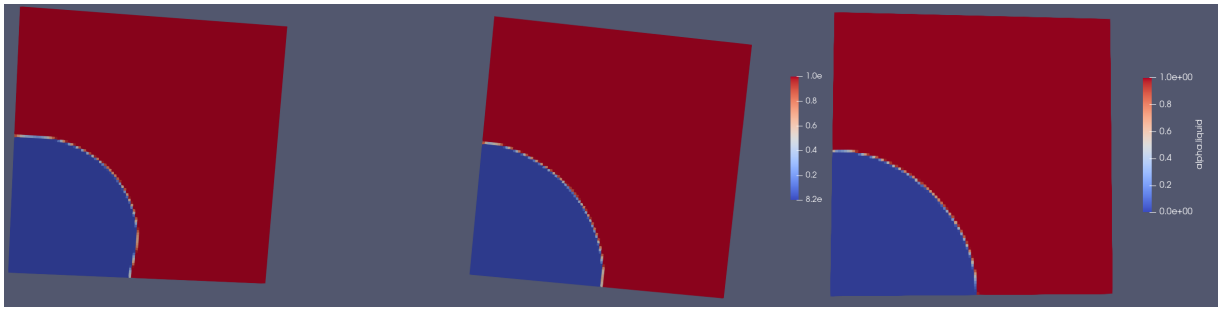

(a) CFL = 1 (b) CFL = 0.2 (c) CFL = 0.02

Figure 3: Comparison of CFL conditions at different settings.

Finally, I attempted to double the size of the initial boundary layer for a square mesh with cells of 2 $\mu$m, see 4. Doubling the initial thermal boundary layer thickness accelerates the computation time since the thermal gradient is smaller when the boundary layer (BL) larger. Initially, the larger BL appears to yield better results. However, the could be due to random variation and futher investiguation is required to confirm this observation. For the remainder of the study, we will keep using the thermal BL determined based on Scriven's theory.

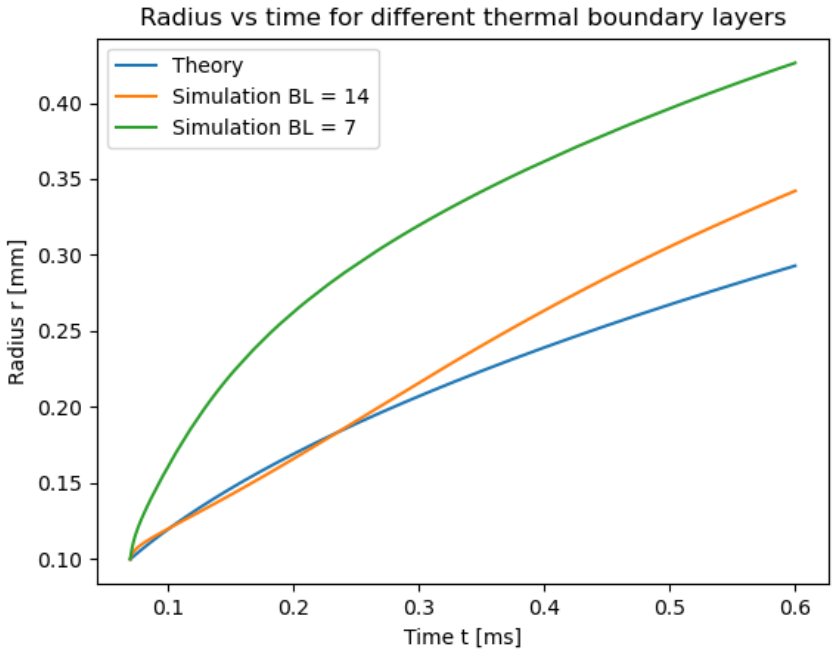


Figure 4: Initial BL impact on the results

### 3.2.2 Mesh convergence

Returning to the initial temperature difference ($\Delta T$) of 5°C, we proceed with mesh convergence testing. For this test case we don't take into account gravity and surface tension. As seen in the Figure 2, a mesh size $\Delta_x$ of 1 $\mu$m, provides precise results but requires 5 hours to simulate just 0.4 ms of bubble growth. A 2 $\mu$m mesh size, though less accurate, reduces the computation time to 45 minutes. A compromise between precision and efficiency has to be found according to what we want to study. Mesh cells of 1$\mu$m result in an error below 5%, whereas mesh cells of 2$\mu$m produce an error of approximately 30%.

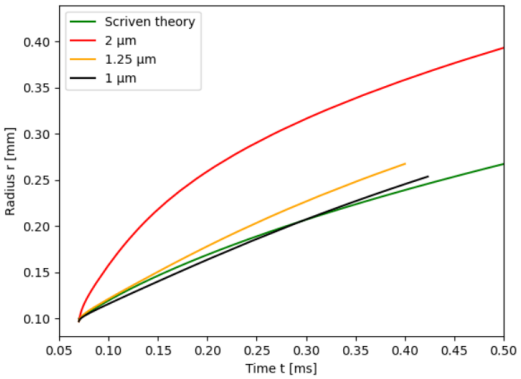


(a) Radius of the bubble convergence

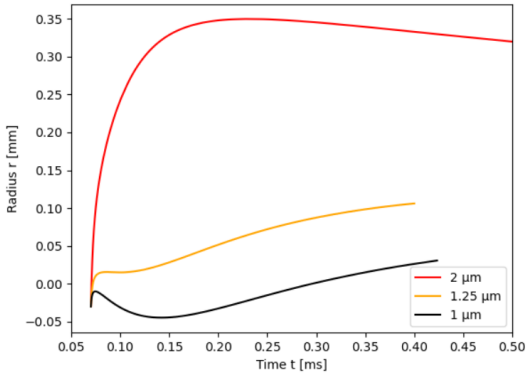


(b) Error in mesh convergence

Figure 5: Comparison of mesh convergence for radius and errors.

### 3.2.3 VOF method and stability

As we observed, there are two primary methods to simulate the impact of surface tension. First, an algebraic VOF (Volume of Fluid) method was tested. However, this approach exhibited instability when incorporating the surface tension force. The source of the instability appears to originate near the axis, likely due to the small dimensions of the cells in the axisymmetric region. Specifically, to improve accuracy, an interface smoothing process is performed, during which terms are divided by the cell face area. In axisymmetric geometries, these areas can be exceedingly small, potentially leading to numerical errors.

Despite attempts to adjust various parameters, the instabilities could not be sufficiently mitigated. Therefore, we ultimately decided to test a geometric VOF method. Although this method also exhibited instabilities that caused unphysical phenomena near the axis (as illustrated in Figure 6), the overall results remained physically and numerically consistent. Consequently, the algebraic VOF MULES (Multidimensional Universal Limiter for Explicit Solution) scheme was selected for the remainder of the study.

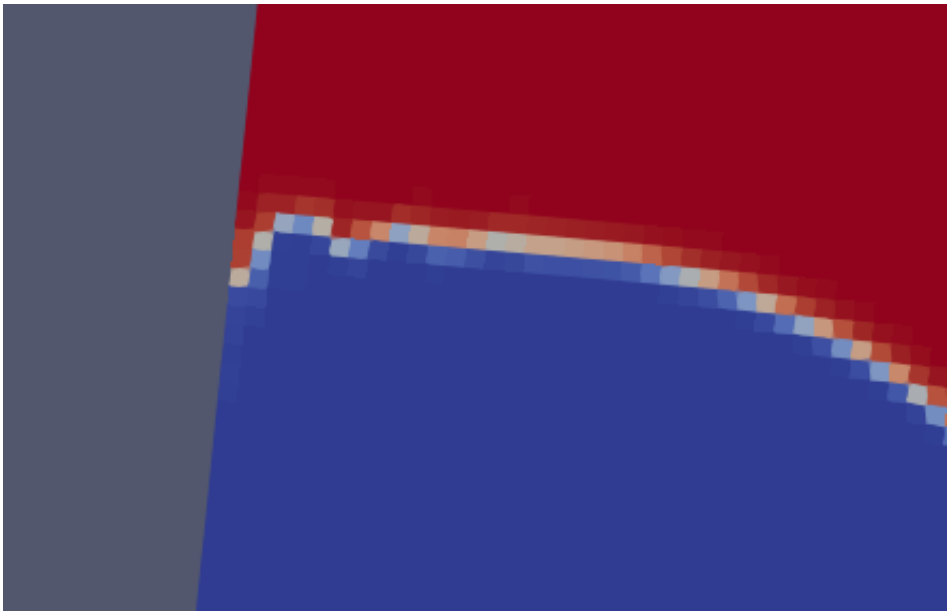

Figure 6: Instability at the interface near the axis

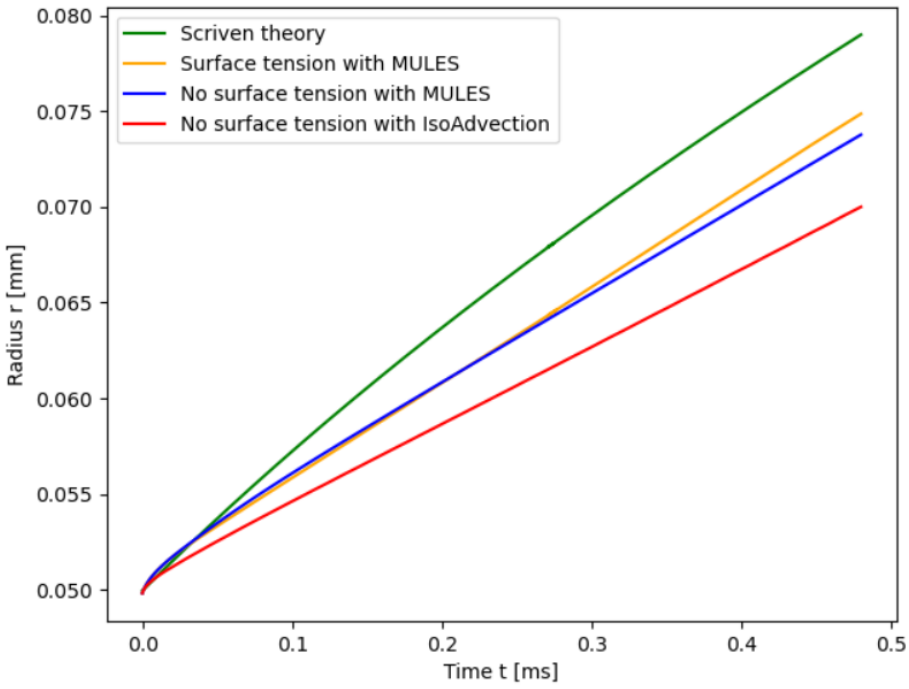


Figure 7: Comparison of various numericals VOF schemes

## 3.3 Study of bubble detachment

### 3.3.1 Setup for bubble detachment

With assurance that our solver provides acceptable results (see Figure 7), and after testing various hypotheses on the parameters to optimize computation time, this section focuses on the bubble detachment process in a pool boiling configuration for saturated R134a.

For this part, we take into account the impact of gravity with an intensity $g = 9.81\,\mathrm{m/s^2}$ and the effect of surface tension.

The computational domain setup assumes the bottom and right faces are walls, while the top face is defined as an outlet. The domain parameters are summarized in Table 2.

Initially, a model is tested using the same parameters as shown in Figure 8. These parameters are detailed in Table 3.

| **Aspect** | **Details** |
|---|---|
| Computational Domain | Axisymmetric, wedge-type geometry representing 5% of the 3D domain, uniform structured mesh, domain size: 0.2 mm × 0.1 mm. |
| Mesh Details | 20,000 hexahedral cells, cell size: 1 $\mu$m. |
| Boundary Conditions (Velocity) | No-slip velocity at solid walls; at outlet: zero gradient for outflow. |
| Boundary Conditions (Pressure) | Fixed flux pressure at solid walls; fixed-value pressure at outlet. |
| Boundary Conditions (Volume Fraction) | Zero-gradient at sidewall and outlet; contact angle of $\theta = 30°$ at lower wall. |
| Boundary Conditions (Temperature) | Bottom wall: constant $T_w = 246.79$ K; sidewall: zero-gradient; outlet: zero-gradient. |

Table 2: Summary of computational domain, mesh, and boundary conditions.

As observed in the study by Georgoulas et al. (Figure 8), the temperature difference between the

| **Phase Properties (R134a at 1 bar, $T_{\text{sat}} = 246.79\,\text{K}$ )** | | | |
|---|---|---|---|
| **Property** | **Unit** | **Liquid** | **Vapour** |
| Density, $\rho$ | $\text{kg m}^{-3}$ | 1377.5 | 5.19 |
| Specific heat, $c_p$ | $\text{J kg}^{-1}\,\text{K}^{-1}$ | 1280.0 | 793.19 |
| Thermal conductivity, $k$ | $\text{W m}^{-1}\,\text{K}^{-1}$ | 0.104 | 0.0093 |
| Kinematic viscosity, $\nu$ | $\text{m}^2\,\text{s}^{-1}$ | $2.76 \times 10^{-7}$ | $1.39 \times 10^{-6}$ |
| Surface tension, $\sigma$ | $\text{N m}^{-1}$ | 0.015 | |
| Latent heat, $h_{lv}$ | $\text{J kg}^{-1}$ | 144,350 | |
| **Initial Conditions** | | | |
| Initial bubble radius | µm | 50 | |
| Initial thermal boundary layer thickness at the wall | µm | 352 | |
| Temperature difference, $\Delta T$ | K | 2.5 | |
| Contact angle | ° | 30 | |

Table 3: Summary of Simulation Parameters

wall and the fluid's saturation temperature has a significant impact on bubble detachment time and diameter.

The higher the wall temperature, the longer the detachment time and the larger the bubble diameter. Due to computational limitations, we chose a small temperature difference of 2.5K for our simulations with R134a. This choice allowed us to use a smaller computational domain and perform simulations over a shorter time frame.

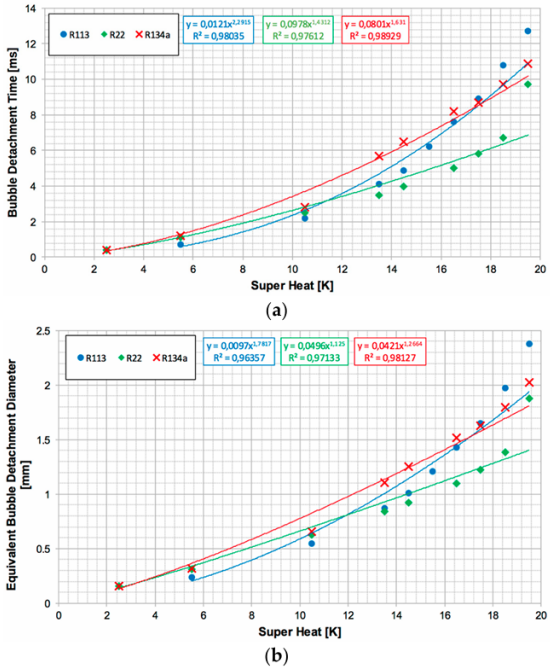


Figure 8: Impact of the wall superheat [3]

In this case, we use the same thermal boundary layer around the bubble as in the bubble growth analysis. Additionally, we introduce a thermal boundary layer at the heated wall to compare our results with those of Georgoulas et al. [3]. This thermal boundary layer, as illustrated in Figure 9, is assumed to have a thickness of 352 $\mu$m.

We model the temperature distribution within the boundary layer using an exponential profile,

ensuring that the boundary layer thickness of 352 $\mu$m corresponds to 99% of the temperature variation between the wall temperature and the saturation temperature. The expression for the temperature profile is given as:

$$T(z) = 246.79 + (249.29 - 246.79) \cdot \exp\left(-\frac{4 \cdot z}{0.000352}\right)$$

The coefficient 4 was determined through multiple tests to ensure the boundary layer thickness matches the expected value.

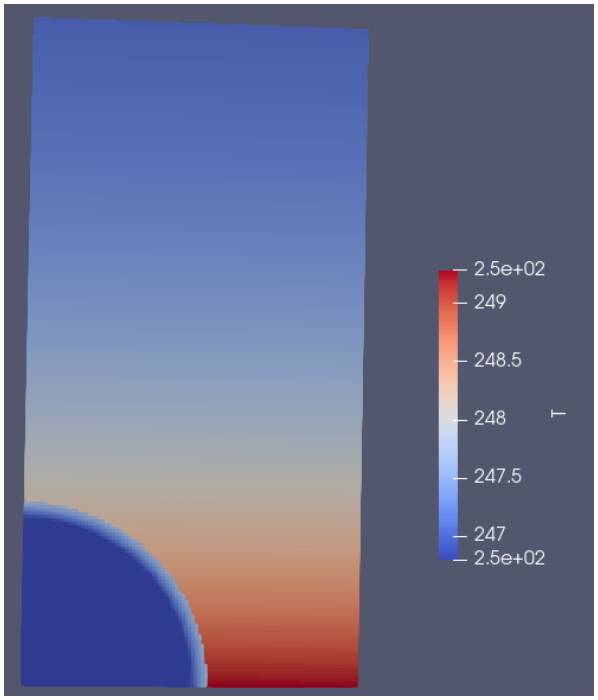


Figure 9: Wall thermal boundary layer

### 3.3.2 Comparison of the results

From Figure 8, we observe that for a 2.5 K superheated wall, the expected bubble detachment diameter is approximately 130 µm, with a detachment time of around 0.4 ms.

Considering the accuracy of our results, we achieve this with an uncertainty of about 10%, which arises from the interpretation of the diagram and the definition of the bubble diameter when the bubble is not perfectly spherical.

### 3.3.3 Impact of various parameters

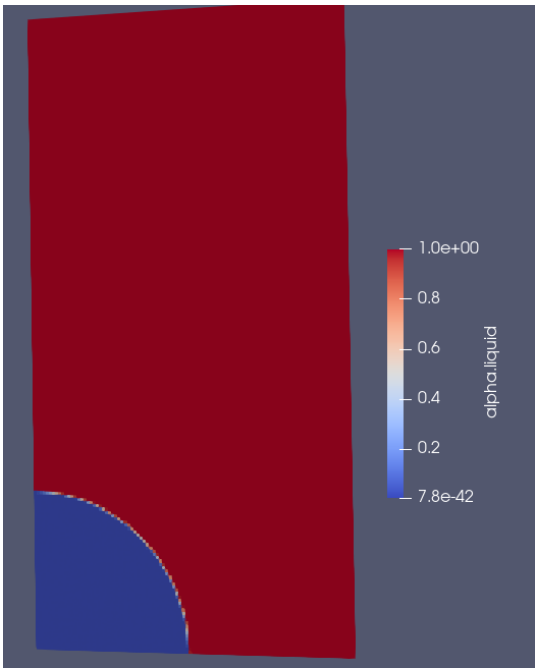


(a) t = 0 $\mu$s

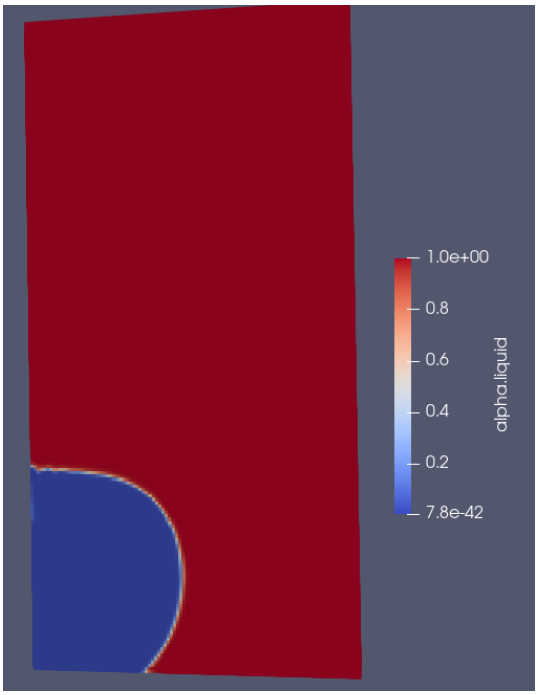


(b) t = 6 $\mu$s

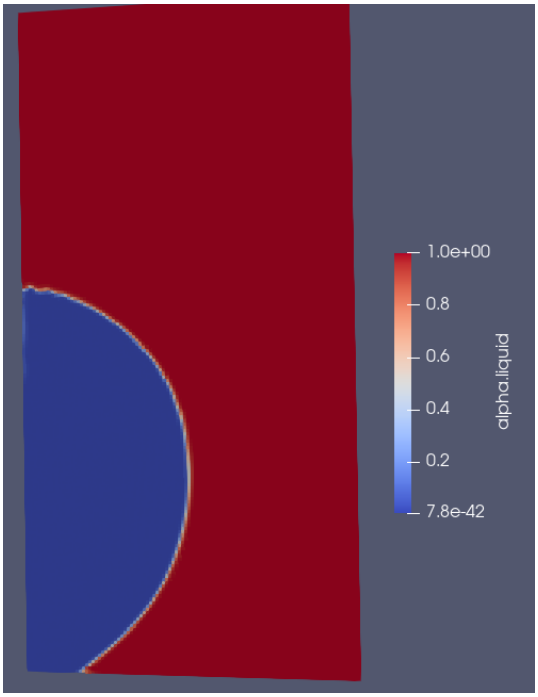


(c) t = 20 $\mu$s

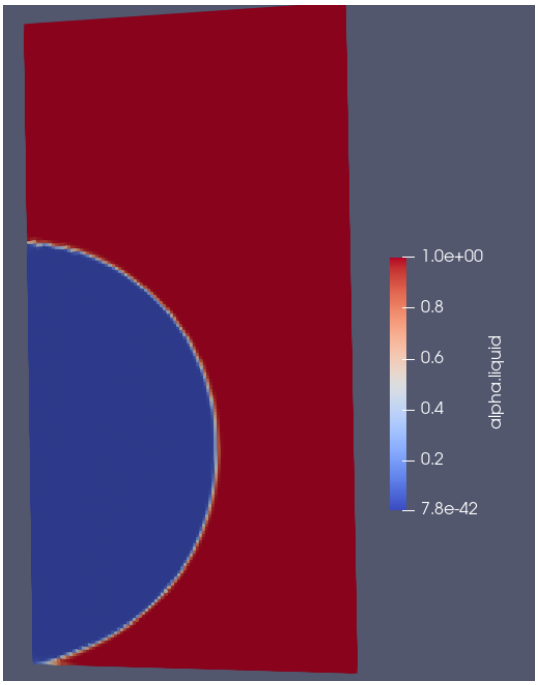


(d) t = 40 $\mu$s

Figure 10: Bubble evolution with time

# References


[1] Fmuni. GitHub - fmuni/boilingFoam-PUBLIC: OpenFOAM-based solvers, libraries, and test cases for simulating boiling flows.

[2] F. Municchi, C.N. Markides, O.K. Matar, and M. Magnini. Computational study of bubble, thin-film dynamics and heat transfer during flow boiling in non-circular microchannels. *Applied Thermal Engineering*, 238:122039, 11 2023.

[3] Anastasios Georgoulas, Manolia Andredaki, and Marco Marengo. An Enhanced VOF Method Coupled with Heat Transfer and Phase Change to Characterise Bubble Detachment in Saturated Pool Boiling. *Energies*, 10(3):272, 2 2017.

[4] Christian Mulbah, Can Kang, Ning Mao, Wei Zhang, Ali Raza Shaikh, and Shuang Teng. A review of vof methods for simulating bubble dynamics. *Progress in Nuclear Energy*, 153:104478, 2023.

[5] J.U Brackbill, D.B Kothe, and C Zemach. A continuum method for modeling surface tension. *Journal of Computational Physics*, 100(2):335–354, 6 1992.

[6] S. Hardt and F. Wondra. Evaporation model for interfacial flows based on a continuum-field representation of the source terms. *Journal of Computational Physics*, 227(11):5871–5895, 3 2008.

[7] L.E. Scriven. On the dynamics of phase growth. *Chemical Engineering Science*, 10(1):1–13, 1959.